

# Mechanical Properties of 316 Stainless Steel Structure produced by Pulsed Micro-plasma Additive Manufacturing

Xiaojing Yuan (✉ [yuanxj2003@163.com](mailto:yuanxj2003@163.com))

xi'an research institute of hi-tech

**Ning Guan**

xi'an research institute of hi-tech

**Xuping Wang**

xi'an research institute of hi-tech

**Hao Li**

xi'an research institute of hi-tech

**Jin Li**

Military Representative Office of rocket army

**Jun Zhan**

Rocket Army Research Institute, Beijing, 100080, China

---

## Research Article

**Keywords:** Pulsed micro-plasma, additive manufacturing, 316 stainless steel, microstructure, mechanical properties

**Posted Date:** August 2nd, 2021

**DOI:** <https://doi.org/10.21203/rs.3.rs-759302/v1>

**License:** © ⓘ This work is licensed under a Creative Commons Attribution 4.0 International License.

[Read Full License](#)

---

# Abstract

An innovative pulsed micro-plasma additive manufacturing (AM) system is proposed for the fabrication of thin-walled 316 stainless steel parts. During the deposition process, the heat accumulation from the micro-plasma can be controlled effectively by adjusting the following parameters: the AM current, pulse length of the plasma arc, and scanning speed. The width of the pool can reach 3.0 mm. The microstructural analysis, micro-hardness tests, and tensile strength tests were performed. The results of the structural characterisation showed that columnar dendrites predominated in the microstructure of thin-walled elements and exhibited epitaxial growth from the bottom to the top and from the middle to both sides, while the top grains had more variations in growth orientation. The grains had a core-shell structure with a growth orientation along the  $\langle 100 \rangle$  direction of the austenite structure, and the boundary was composed of migrated C and Cr. The micro-hardness of the thin-walled structure (240–320 Hv<sub>0.3</sub>) decreased with increasing the deposition thickness. The tensile strength and yield strength of the thin-walled parts were 669 and 475 MPa, respectively. The fracture mechanism was that cracks formed along the pores along the pores of the grain boundary and then propagated along them, ultimately leading to the fracture.

## 1. Introduction

Additive manufacturing (AM) techniques accumulate material layer by layer using a computer-aided design/computer-aided manufacturing (CAD/CAM) model to develop three-dimensional (3D) products in or near their final shape unlike the traditional subtractive metal manufacturing.<sup>1–3</sup> AM techniques allow the production of the complex parts with less material and energy loss, have a short processing cycle, and are convenient for the rapid processing of spare parts in the battlefield environment. Therefore, AM technology has become an important topic in the field of military equipment support<sup>4</sup>.

Today, AM processes use a laser beam, electron beam, arc, or plasma as the heat source, and the feedstock is in the form of a powder, wire, or sheet<sup>5,6</sup>. As a comparison, selective laser sintering/melting (SLS/SLM), laser engineering net shaping (LENS), direct laser fabrication (DLF), and binder jet 3D printing have been investigated for manufacturing the parts<sup>7</sup>. However, scientists still try to improve manufacturing efficiency and reduce equipment costs to promote the implementation of AM technology to more fields.

Compared to the powder-based laser AM process, the innovative pulsed micro-plasma AM (MPAM) technique, which employs a controlled micro-plasma as the heat source, has the potential to fabricate large fully dense parts with relatively low manufacturing costs and high efficiency. The molten powders are deposited on a substrate, solidify at the boundary of the melt pool, and form the designed parts layer by layer. The micro laser metal wire deposition (LMWD) process is studied as an additive manufacturing process for manufacturing thin walled structures with high aspect ratio.<sup>8</sup>

Stainless steel, which contains the austenitic phase, is important. It has been widely used in the machinery manufacturing, chemical industry, and other fields owing to its excellent mechanical properties and corrosion resistance<sup>9,10</sup>. Currently, casting methods, involving tedious procedures such as moulding, are employed to fabricate stainless steel parts with unique shapes in small production batches. Recently, Sun *et al.*<sup>11</sup> used an optimised SLM process to manufacture high-density parts (99%) with a 72% increase in productivity. De Lima *et al.*<sup>12</sup> fabricated a 316L stainless steel part with a single-phase austenitic structure, and its performance index reached expectations. Lin *et al.*<sup>13</sup> fabricated a 316L stainless steel component using the AM technique and studied several aspects, such as the phase formation, layer formation, and continuous columnar grain growth. They showed that during the rapid prototyping, single-phase austenite ( $\gamma$ ) dendrites grew. There were clearly pronounced layered structures between different cladding layers, which further clarified the mechanism of the continuous epitaxial columnar grain growth during the manufacturing process. Technological research has shown that the tensile strength of a part along the scanning direction was higher than that in the other directions. In addition, the component exhibited optimal plasticity. With the use of the end deceleration, reduced heat input, direct water cooling, and optimised scanning pathways, the improved parts can be obtained<sup>14,15,16</sup>. The large thermal effects limit the fabrication of 316L stainless steel components using AM techniques<sup>17,18,19</sup>.

In this study, AISI 316 thin-walled parts were produced using the pulsed MPAM technique. The microstructure of the bottom, middle, and top sections were analysed and the corresponding mechanical properties were measured. The phase structure and mechanical properties of the obtained parts were compared to those of the base metal fabricated using the traditional rolling forming process.

## 2. Experimental Materials And Methods

### 2.1 Experimental materials

The AISI 316 stainless steel powder used in the experiment was obtained from *Tianjin Zhujin Technology Co.* and is shown in Fig. 1. The chemical composition of the stainless steel powder is presented in Table I. The particle size was measured using a laser particle characterisation analyser (*LS 230, Fluid Module*). The powder exhibited good fluidity for good periodisation and the mean particle size was approximately 53  $\mu\text{m}$  (Fig. 1(b)), showing that the AISI 316 stainless steel powder was suitable for MPAM.

**Table I** Chemical composition of the AISI 316 stainless steel powder (wt. %)

C	Cr	Mo	Ni	Mn	Si	Fe
0.08	18.02	2.23	10.61	0.37	0.98	Balance

**Figure 1** Microstructure of the AISI 316 stainless steel powder: (a) SEM image of particles morphology and (b) particle size distribution

## 2.2 Deposition process

In this study, the pulsed MPAM system (shown in Fig. 2(a) and (b)) included a metal powder micro-plasma depositing system with water cooling, a ZNC-2300D fixed-arm CNC platform, a control platform, and a shifting device. As shown in Fig. 2(a), the positioning machine and fixed-arm CNC machine provided precise control of the overlay AM process. Various parameters, such as the AM current, powder feeding speed, and scanning speed, were controlled, and the path planning function was achieved (Fig. 2(b)). Q235 steel was selected as the baseplate with the dimensions of 120 × 80 × 40 mm. A thin-walled specimen with the dimensions of 60 × 60 × 30 mm and the wall thickness  $\sim 3 \pm 0.3$  mm designed to be fabricated with AISI 316 stainless steel is shown in Fig. 2 (c).

**Figure 2** (a) Schematic and (b) photograph of the MPAM system; (c) design of the thin-walled AISI 316 stainless steel parts; (d) optimised MPAM process; and (e) 316 stainless steel thin-walled sample taken for microstructural analysis and micro-hardness measurements

The optimised parameters for the MPAM pulse process are listed in Table II. Where, the Ar<sub>2</sub> gas was used as protective feed gas during the experiment. The optimal MPAM process was determined, as shown in Fig. 2 (d), in which the micro-plasma current decreased stepwise because of an increase in the accumulated heat. When the initial AM current is 100A, the deposited 316 stainless steel layer can be obtained. However, Due to the increase of heat accumulation, a large number of deposits will melt. Therefore, according to the absorption of heat, the step current is used to control the heat of plasma, such as 100A for 600s, 88A for 1020s, 70A for 480s, 60A for 1800s and 55A for 3900s. In addition, the optimal scanning speed of Micro-plasma gun with experiment is 140 mm/min, 200 mm/min, 350 mm/min, 750 mm/min and 1050 mm/min, respectively.

**Table II** Primary parameters for pulsed MPAM

Parameter	Value	Parameter	Value
Micro-plasma current (A)	10	Baseplate dimensions (Q235 steel, mm)	120 × 80 × 40
AM current (A)	100→88→70→60 →55	Ion gas flow (Ar <sub>2</sub> , L/min)	1.0
Base current (A)	10	Protective gas flow (Ar <sub>2</sub> , L/min)	10
Current rise time for pulse arc (s)	0.1	Powder feeding gas flow (L/min)	4.5
AM interval for pulse arc (ms)	50.0	AM time for pulse arc (ms)	90.0
Gas protection time (s)	6.0	Load duration (%)	60
Input voltage (V)	380 AC, 50 Hz	Specific flow of cooling water (m <sup>3</sup> /h)	1
Specific power capacity (kVA)	17.8	Cooling capacity (W)	5200
Output current regulation range (A)	1-300	Micro-plasma gun scanning speed (mm/min)	140→200→350 →750→1050

## 2.3 Microstructural characterisation

The microstructure of the samples was characterised using scanning electron microscopy (SEM) with energy dispersive spectroscopy (EDS) and Electron Backscattered Diffraction (EBSD)(Hitachi S3400N). **Where, EBSD was used to analyse the texture, grain size and grain orientation difference, respectively.** EBSD samples were prepared by rough grinding, fine grinding, polishing, and vibration polishing and other processes. Vibration polishing for 2-5h can effectively remove the residual stress on the sample surface, and the EBSD test step was set to 5µm.

The compositions were analysed using a Lab X' Pert-Pro MPD X-ray diffractometer with Cu K $\alpha$  radiation with a scan rate of 0.04°/min and the 2 $\theta$  angle ranging from 20° to 100°. As shown in Fig. 3, indentations were made along the centre line in both the horizontal and vertical directions.

The composition and properties of the AISI 316 thin-walled structure were obtained employing X-ray photoelectron spectroscopy (XPS, Axis Ultra (UK)), using monochromatic Al K $\alpha$  (150 W, 15 kV, 1486.71 eV) and the vacuum of 10<sup>-9</sup> torr. The binding energies were calibrated relative to the C 1s hydrocarbon peak at 284.8 eV, which was assigned to the species absorbed on the surface of the sample.

## 2.4 Mechanical property tests

The hardness tests were performed with an HVS-1000 2 micro-hardness tester with a load of 300 g and a loading time of 10 s. According with ISO6892:2009 standard, the mechanical tensile was performed at room temperature using an INSTRON 5982B18430 tensile tester. Where, the sample size was 15×10×3 mm. The tensile test conditions were a gauge distance of 4 mm and tensile rate of 0.075 mm/min. The entire tensile testing process was monitored and recorded.

As a pre-treatment method, the sample was obtained from the thin-walled parts using wire electrical discharge machining and grounded with sandpaper. Subsequently, the sample was polished with 5–0.5 µm diamond polishing agents. The sample was corroded in a 10% HCl, 10% HNO<sub>3</sub>, and 15% cold acetic acid solution for 30 min. Finally, the sample was washed with alcohol to remove the corrosive solution and left to air dry.

## 3. Results And Discussion

### 3.1 Deposition process of thin-walled AISI 316 stainless steel

Figure 3 shows the MPAM process. To improve the deposition quality, the characteristics of the pulsed micro-plasma column, such as the AM current, powder feeding speed, and scanning speed, were mainly adjusted according to the shape of the molten pool, as shown in Fig. 3(a) and (b).

During the deposition process, the optimised current of the pulsed micro-plasma and the operation time were 100 A (600 s), 88 A (1020 s), 70 A (480 s), 60 A (1800 s), and 55 A (3900 s). The scanning speed of the micro-plasma nozzle was 140 mm/min for 35 min, 200 mm/min for 30 min, 300 mm/min for 5 min, 350 mm/min for 5 min, 400 mm/min for 5 min, 750 mm/min for 15 min, and 1050 mm/min for 35 min (shown in Fig. 2(d), respectively). The optimised pulse time of the micro-plasma was 90 ms and the AM interval for the pulsed micro-plasma arc was 50 ms. The temperature of the ion arc during the deposition was considerably higher than that during the AM interval for the pulsed micro-plasma. Thus, energy can be effectively reduced.

During the growth process of the thin-walled AISI 316 parts, the molten pool remained stable, and the temperature of the deposition layer decreased with increasing the distance from the plasma arc column. This shows that the pulse time of the micro-plasma arc (90 ms) was optimized, which effectively prevented excess energy accumulation, the thin-walled parts from overheating or even collapsing during the deposition process and ensured that the molten pool was continuously maintained (Fig. 3(b)). The fabricated AISI 316 thin-walled parts was a thin-walled, square-shaped structure with a height of 22 mm and a length/breadth of 60 mm.

The optimised process had better control over the accumulated heat by adjusting the pulse duration of the plasma arc, which regulated the width of the molten pool and the height of the cladding layer. This ensured a reliable metallurgical connection between the middle layer and the layer in the AM process and

prevented the structural failure because of overheating. Regarding the macrostructure of the thin-walled members, there was no clear stacking on the inner and outer surfaces, there was no significant difference in the covering width of the thin-walled structures, and the overall stiffness was good. Because of the temperature control, some particles were not fully melted in the molten pool, and these semi-melted particles accumulated on the surface of the thin-walled structure, forming a spherical growth at high temperature. Upon thermal accumulation in the thin-walled structure, thermal inhomogeneity led to distinct fluctuations in the top deposition layer. There were different degrees of collapse and deflection at the corner. The heat accumulation on the inner surface of the structure was more prominent than that on the outer surface. The geometric characteristics of the thin-walled inner surface layer were clear, while the outer surface appeared relatively flat.

**Figure 3** Pulsed MPAM process: (a) micro-plasma arc; (b) thin-walled AISI 316 stainless steel made by pulsed MPAM

In this study, the thin-walled AISI 316 parts fabricated by MPAM had a smooth and regular layered surface structure, showing a typical cladding form. Compared with the thin-walled structure made by laser-assisted MIG arc AM <sup>18</sup>, the thin-walled structure formed by this technology had a better bonding strength. However, it was also found that upon growing a thin wall, a hot stress concentration point appeared at the corner, which quickly led to overheating of the thin-walled structure and its collapse. These results show that the optimisation of the deposition process and the planning of the trajectory of the micro-plasma nozzle are of great engineering importance for the construction of high-quality structures.

## 3.2 Microstructural evolution of the thin-walled structure

The microstructure of the thin-walled structure is shown in Fig. 4. There was layered structure in the microstructure of the AISI 316 stainless steel (Fig. 4(a)). The deposition layer in the middle of the parts had a horizontal layered structure and the crystal structure consisted mainly of columnar dendrites, showing a metallurgical combination. The thin-walled parts had neither porosity nor any defect inclusions, unlike the microstructure of the ones obtained with the AM laser <sup>10</sup>. Figure 4(b-d) shows the microstructure of the thin-walled parts along the deposition (vertical) direction. The heat accumulation effect influences the characteristics of the microstructure. In the initial deposition stage (Fig. 4(b)), because of the rapid heat dissipation, the nucleation rate of grains was higher than the growth rate; thus, the microstructure comprised small and dense columnar crystals.

**Figure 4** microstructure of various positions in the sample of the fabricated parts: (a) low-magnification SE image of the local position, (b) bottom zone of the deposited sample, (c) middle zone of the deposited sample, and (d) top zone of the deposited sample; (e) SEM of the layer zone (in the middle zone, shown in) and (f) XRD pattern of the AISI 316 stainless steel thin-walled parts and powder. (g-i) EBSD of (b,c) and (d), respectively; **(j) the inverse pole figures of bottom area and top area, respectively.**

During the continuous deposition (Fig. 4(c)), the temperature gradient and solidification rate were stable throughout the moulding process, and the structure mainly comprised columnar crystals with small dendrites and some transverse crystals.

At the top of the thin-walled parts (Fig. 4(d)), the nucleation rate decreased and the change in thermal gradients and the direction of the grain growth changed accordingly. The structure contained the columnar crystals with complex orientations and the number of the transverse crystals increased markedly. During the deposition, the distance between the primary dendrites increased markedly and the secondary dendrites developed gradually. This shows that the accumulation of plasma energy had a large effect on the thin-walled parts; in particular, the rate of solidification decreased when the temperature was kept constant.

There is a distinct core-shell structure at each phase boundaries, as seen in Fig. 4(e). Also, this ferrite-containing austenite structure was formed on the grain surface, which can be proved with Fig. 4(i). The results show that the growth of ferrite along the vertical direction was limited, and it was primarily present in the form of a network. This is because during the solidification ferrite grows towards the negative temperature gradient. Near the surface, the ferrite had better growth conditions and grew along the surface toward the centre of the molten pool. The solidification speed in the middle part of the sample was slow, which restrained the growth of ferrite; thus, ferrite was mainly present in the network. Near the substrate, the energy input of plasma was transmitted rapidly through the substrate. The microstructure in this position was controlled by the rapid solidification of the melt pool.

Figure 4(f) shows the X-ray diffraction (XRD) pattern of the AISI 316 thin-walled specimen formed by MPAM. The XRD results show that it had a fully austenitic single-phase structure; however, in the SEM, the cell-like and columnar substructures were observed, which were nearly hexagonal and elongated hexagonal, and uniformly distributed inside the grains. Unlike the traditional AISI 316 stainless steel, the structure of the formed samples consisted of the FCC solid solution with the preferred growth orientation of  $\langle 100 \rangle$ . It was found that  $\text{Cr}_2\text{O}_3$ ,  $\text{Cr}_2\text{C}_3$ , and some amorphous materials were also formed during the deposition.

In addition, the EBSD images were obtained at the bottom zone and top zone of the deposited sample, shown in Fig. 4 (g and h). Where, the cell/dendrite boundaries can be mixed up with grain boundaries. **It can be seen that as the layer height increases, the proportion of red in the image gradually decreases and the proportion of blue gradually increase. It can be found that the  $\text{Cube}\{100\}\langle 001 \rangle$  texture is mainly used in the bottom area, and the crystal orientation is very obvious. At the top area, the silk texture of  $\langle 111 \rangle$  gradually increased. In addition, the inverse pole figure of top area and bottom were shown in Fig. 4(i). It illustrates that the texture strength of  $\langle 001 \rangle$  gradually decreased from 9.106 to 4.157, which proved that the dominant position of  $\langle 001 \rangle$  texture was gradually lost. The strength of  $\langle 101 \rangle$  and  $\langle 111 \rangle$  orientations in the top area gradually increased, and preferred orientation of equiaxed crystals gradually decreased.**

### 3.3 Characterisation of an individual grain

As mentioned previously, the microstructure of the thin-walled parts prepared using pulsed MPAM technology differed from that of traditional manufacturing. As shown in Fig. 5(a) and (c), there was a distinct core-shell structure at each grain boundary. It may be utilised to determine the orientation-dependent lattice parameters with sufficient accuracy to assess the phase strain evolution between austenite and ferrite <sup>21</sup>.

The dendrite (spectrum A) had a single-phase austenite structure with a typical elemental composition and atomic ratios (Fig. 5(b)). Owing to the large temperature gradient during the rapid directional solidification, micro-segregation between the dendrites (spectrum B) was unavoidable. It can be observed in Fig. 5(d) that the C and Cr concentrations increased considerably.

**Figure 5** (a) SEM image and (b) EDS profile of the dendrite in point A. (c) SEM image and (d) EDS spectrum of the interdendritic region in point B.

The energy spectrum analysis for various regions is listed in Table 3. Region A corresponds to the interior of an individual grain, and Region B corresponds to the boundary of the individual grain. Compared with the AISI 316 stainless steel powder, the average C concentration in the boundary region was 2.33 fold, and the Cr concentration was 2.14 fold that of the grain. In addition, oxygen was found at the boundary. This indicates that due to the high temperatures during the AM process, C and Cr atoms moved from the interior of the grain and aggregated on the grain boundary, forming carbides and oxides with Cr and Fe in the oxygen-containing environment. It can be seen that the microstructure of 316 stainless steel produced by additive appears segregation, and the content of Cr, Mo and Ni between dendrites is higher than that in dendrites, listed in Table 3.<sup>22</sup>

**Table 3** Energy spectrum analysis for various regions

No.	Region	Atom fraction of the element (at. %)								
		C		Cr		Fe	Ni	Mo	O	Si
1	Spectrum A	0.47	Mean value	18.16	Mean value	67.49	10.13	0.75	-	-
2		0.25	<b>0.278</b>	18.91	<b>18.534</b>	66.48	11.29	0.79	-	2.29
3		0.21		18.65		68.40	10.36	0.63	-	1.76
4		0.34		19.22		66.73	10.70	0.93	-	2.08
5		0.12		17.73		68.51	10.75	1.03	-	1.85
6	Spectrum B	0.67	Mean value	37.45	Mean value	52.47	6.47	2.64	-	-
7		0.68	<b>0.648</b>	32.59	<b>39.696</b>	47.83	5.6	2.59	9.35	1.38
8		0.51		41.36		48.79	4.98	4.09	-	-
9		0.59		48.25		45.00	3.63	2.33	-	0.20
10		0.79		38.83		51.30	4.58	3.63	-	0.44

The composition and properties of the samples fabricated by MPAM were revealed by X-ray photoelectron spectroscopy (XPS). Figure 6 shows the peaks of Fe2p and Cr2p at 707.40 and 574.36 eV, respectively (listed in Table I). According to the XRD pattern, oxides and carbides with the structure  $Cr_xC_y$  (e.g.,  $Cr_{23}C_6$ ) and  $Cr_2O_3$  gradually formed at the high temperatures during the AM process. In addition, elemental segregation causes performance fluctuation, which can be solved by subsequent aging heat treatment.

**Figure 6** XPS profiles of the surface of the thin-walled AISI 316 stainless steel parts

**Table I** Elemental identification and quantification

Element	Peak position (eV)	Area (CPS•eV)	at. %
Fe2p	707.40	3367684.48	38.86
Cr2p	574.36	599147.42	7.72
Ni2p3	853.19	319637.06	4.20
O1s	531.71	124366.31	6.38
Na1s	1072.75	54883.52	1.23
Mo3d	228.38	99634.81	

The  $\chi$  phase peaks decreased gradually with increasing temperature. When the temperature increased, new diffraction peaks from the body-centred cubic structure emerged, while the ferrite phase increased

markedly and the  $\sigma$  phase and  $\chi$  phase disappeared. Owing to the composition of steel (high Cr and Mo concentrations), the  $\sigma$  phase and  $\chi$  phase (an equivalent intermetallic phase rich in Cr and Mo) typically precipitate in the substrate, forming a poor alloy area that reduces the corrosion resistance of the material.

### 3.4 Hardness distribution in the thin-walled structure

The hardness values at different locations are listed in Table II. The hardness of the bottom, middle, and top parts of the thin-walled structure were  $299.53 \pm 15.3$  Hv,  $291.7 \pm 28.2$  Hv, and  $281.5 \pm 36.7$  Hv, respectively, indicating the decrease in the hardness of the thin-walled parts as the structure was deposited, which was related to the effect of heat accumulation.

**Table II** Micro-hardness of thin-walled AISI 316 stainless steel (300 g, 10 s)

Sample No.	Measured value (Hv <sub>0.3</sub> )		
	Top	Middle	Bottom
1	314.6, 287.2	307.9, 282.7	204.5, 275.6
2	285.7, 299.6	314.7, 277.0	307.8, 330.8
Mean value	296.75	295.56	279.7

**Combined with Fig. 2(e)**, the hardness distribution of the thin-walled parts was tested in the vertical section to understand the influence of the MPAM process on the performance of the thin-walled parts; the horizontal direction was sampled in steps of 0.2 mm and the vertical direction in steps of 0.6 mm. The hardness distribution in both directions is shown in Fig. 7.

The micro-hardness distribution in the horizontal and vertical (growth) directions in the middle position are shown in Fig. 7(a) and (b), with the values of 240–320 Hv and 290–320 Hv, respectively. It is observed that **the hardness of the thin-walled parts manufactured by pulsed MPAM was in the range of 240–320 Hv. In the horizontal direction, the hardness near the edge of the thin-walled structure was higher, and the hardness outside was higher than that inside;** in the vertical direction, the hardness near the surface fluctuated most noticeably, showing that the hardness of the grains decreased because of the heat accumulation in the structure. In addition, the regions with high hardness could be the ceramic particles on the grain boundary. In the AM process, heat dissipation at the centre and top of the parts was slow, leading to the coarsening of the grain and decrease in the hardness. In contrast, the temperature gradient at the edge was relatively large, the solidification rate was high, and the grains were refined, resulting in high hardness.

**Figure 7** Micro-hardness distribution in the AISI 316 stainless steel parts fabricated by the pulsed MPAM process: hardness distribution in (a) the horizontal direction; (b) the vertical direction

### 3.5 Mechanical properties of the AM sample

A section of the moulded part was taken perpendicular to the scanning direction. The sample was prepared using wire electrical discharge machining technology (Fig. 8).

The mechanical strength was measured using a universal tensile tester. The tensile properties of the solution-annealed samples tested at room temperature are listed in Table II. It is note that the tensile section area of sample 1 was out of tolerance, resulting in a non-uniform stress distribution across the parts and eventually in bending issues. The sample was again prepared and tested to measure its mechanical properties using the same fabrication methods and surface grinding/polishing treatment.

The tensile strength ( $R_m$ ) of the AISI 316 stainless steel sample deposited by pulsed MPAM was 669 MPa and the yield strength ( $R_{P0.2}$ ) 475 MPa. Thus, the mechanical strength of the parts fabricated using the pulsed MPAM technique was considerably higher than that fabricated by the traditional method. Compared with Laser AM process and Arc AM process, this process is providing any advantages in terms of the properties.

Obviously, similar to the mechanical properties of thin-walled parts manufactured by MIG additive manufacturing, the tensile strength of thin-walled parts manufactured by pulsed micro-plasma additive manufacturing in the vertical direction is less than the tensile strength in the horizontal direction, showing anisotropic characteristics. It can be inferred that the vertical tensile strength of thin-walled parts manufactured by pulse micro-arc plasma additive manufacturing should be reach 600MPa.

**Table II** Mechanical properties of the AM sample

Sample No.	tensile strength $R_m$ (MPa)		yield strength $R_{P0.2}$ (MPa)	$A_{10mm}$ (%)
Pulsed Micro-plasma AM	479	600	276	41.9
	669		475	-
	652		450	33.5
Roll forming [23]	604		266	51
Laser AM[24]	692			21
Arc AM[25]	601			43.3
MIG arc Additive[26]	Vertical	537.32	302.18	43.22
	Horizontal	580.51	305.84	43.12
Boll	480		177	40

**Figure 8:** Schematic diagram of micro-plasma additive manufacturing parts and sampling and testing dimensions (unit: mm).

**Figure 9** Microscopic images revealing the morphology of the fractured sample: (a) fracture surface, (b) dispersed particles in the fracture surface; and (c) and (d) typical dimple-like structure

Figure 9 shows the fracture morphology of the thin-walled parts. Combined with Table 6, the above results exhibit the necking phenomenon in the tensile section. The elongation of the samples was 41% and tensile fracture yielded a typical dimple structure according to the micromorphology of the fracture surface (see Fig. 9(c)), indicating the ductile fracture mode of the thin-walled structure. However, there were fluvial patterns (Fig. 9(a)) and a few independent particles (Fig. 9(b)) on the fracture surface, showing that there was also a small amount of brittle fracture. Figure 9(b) and (d) demonstrates that the crack was affected by the temperature gradient in the AM process. The solidification gradient in thin-walled parts was leading to the segregation with a high concentration of C and Cr at the grain interface and carbides and oxides were formed at a high temperature in the oxidising environment.

In summary, the AISI 316 stainless steel thin-walled parts made by pulsed MPAM had high toughness and high strength. The fracture mechanism is as follows: the crack occurs along the grain boundary pores and propagates along the grain boundary, finally leading to the fracture.

According to the characteristics of the development of pulsed micro-arc plasma additive manufacturing technology, its additive manufacturing speed is at the forefront of the current additive manufacturing technology. However, the heat concentration must be controlled by the pulse width or optimized by printing path planning. In addition, affected by the diameter of the arc spot of the pulsed plasma arc, the printing accuracy and resolution of additive manufacturing is lower than that of laser additive and electron beam additive technology. Although, from the perspective of overall technological development, plasma additive technology is one of the technologies that will inevitably develop in the field of additive manufacturing due to its high forming rate and sufficient energy.

## 4. Conclusion

AISI 316 stainless steel thin-walled components were fabricated with a home-built pulsed MPAM system. The microstructural analysis, micro-hardness tests, and tensile strength tests were performed. The results are as follows:

- By regulating the AM current, pulse length of the plasma arc, and scanning speed, heat accumulation in the MPAM process can be controlled effectively. The deposition pool for the thin-walled parts presents horizontal accumulation, without melt collapse, porosity, or inclusion defects.
- Owing to the influence of heat dissipation, the microstructure of the thin-walled parts was dominated by the columnar dendrites, which exhibited epitaxial growth from the bottom to the top and from the middle to both sides, and the top grains had more variation in growth orientation. From the combination of the XRD and XPS analyses, it was deduced that the grains had a core-shell structure with a growth orientation along the  $\langle 100 \rangle$  direction of the austenite structure, and the boundary was composed of migrated C and Cr.

- The micro-hardness of the thin-walled structure decreased with increasing the deposition thickness and was between 240 and 320 Hv<sub>0.3</sub>. The tensile strength and yield strength of the thin-walled parts were 669 and 475 MPa, respectively. The fracture mechanism is as follows: the crack forms along the pores of the grain boundary and propagates along the grain boundary, finally leading to fracture.

## Declarations

### Acknowledgments

This study was supported by the Scientific Research on Military Maintenance Reform Project (No. WG20211031).

### Author Contributions

**Yuan Xiaojing** performed the modelling and wrote the manuscript; **Guan Ning** contributed to the optimisation and analysis of the data; **Wang Xuping** and **Li Hao** designed and performed the milling experiments; **Jin Li, Jun Zhan** performed the experiments and analysed the data.

### Conflicts of Interest

The authors declare no conflict of interest.

## References

1. Mikel Casuso F, Veiga A, Suárez, etc., *Metals*, 2021, 11(5), 678
2. Vittoria Laghim M, Palermo G, Gasparini, eta., *Journal of Constructional Steel Research*, 2020, 167, pp.105858
3. Wang Z, Palmer TA, Beese AM (2016) *Acta Mater* 110:226–235
4. Tolosa I, Fermín Garcíandía, Zubiri F (2010) et al.. *Int J Adv Manuf Technol* 51(5–8):639–647
5. Segura IA, Mireles J, Bermudez D, Terrazas CA, Murr LE, Li K et al (2018) *Journal of Nuclear Material* 507:164 ~ 176
6. Atefeh Aramian SM, JavadRazavi Z, Sadeghian, *Additive Manufacturing*, 2020, 33, pp.101130
7. Miao Q, Wu D, Chai D, etc., *Materials and Design*, 2020, 186, pp. 108205
8. Demir AG (2018) *Opt Lasers Eng* 100:9–17
9. Mayur S.Sawant NKJain, Sagar HNikam, *International Journal of Mechanical Sciences*, 2019, 164, pp.105166
10. Sun Z, Tan X, Tor SB, et al. *Materials & Design*, 2016, pp.:S0264127516306372
11. Jessrie Dilag T, Chen S, Li SA, Bateman (2019) *Additive Manufacturing* 27:167–174
12. De Lima MSF, Sankaré (2014) *Simon Materials Design* 55:526–532
13. Lin X, Yang HO, Chen J, Huang WD (2006) *Journal of Metals* 04:361–368

14. Ujkaisi Ayiti. Modern Manufacturing R Engineering, 2012, 04, pp. 78–80.(in Chinese)
15. Urikaisi Ayiti. Machine Tools and Hydraulics, 2012, 40, 13, pp.19–21. (in Chinese)
16. Martina F, Mehnen J, Williams SW et al (2012) J Mater Process Technol 212(6):1377–1386
17. Davies HM, Mehmood S, Khaliq A, et al (2017) Microsc Microanal 23:S1, pp. 404–405
18. Buican G, Răzvan, Oancea G, Lancea C et al. Applied Mechanics and Materials, 2015, 809–810, pp. 369–374
19. Nagy J, Huang X. American Society of Mechanical Engineers Digital Collection, 2018(1)
20. Zhang Z, Sun C, Xinkun XU, Liming (2018) Liu International Journal of Lightweight Materials Manufacture 1:89–95
21. Brown DW, Losko A, Carpenter JS, Cooley JC, etc. Metallurgical and Materials Transactions A, 2019, 50, pp. 2538–2553
22. Rong-qing ZHOU, Wei-lian SUN, Yu-ting JIA (2017) Transactions of Materials Heat Treatment 38(4):106–111 (in Chinese)
23. Buican G, Răzvan, Oancea G, Lancea C, et al. Applied Mechanics and Materials, 2015, 809–810, pp. 369–374
24. CHENG Ling-yu, Zhao-hui HE, Jing SUN, etc. Laser & Infrared, 2021, 21, 5, pp. 171–177(in Chinese)
25. Liming LIU, Yajing HE, Zongyu LI, etc. Transactions of The China Welding Institution, 2020, 41, 12, pp.13 – 19(in Chinese)
26. Jin Hu, Master's Thesis of Xiangtan University, 2020, pp.78–90(in Chinese)

## Figures

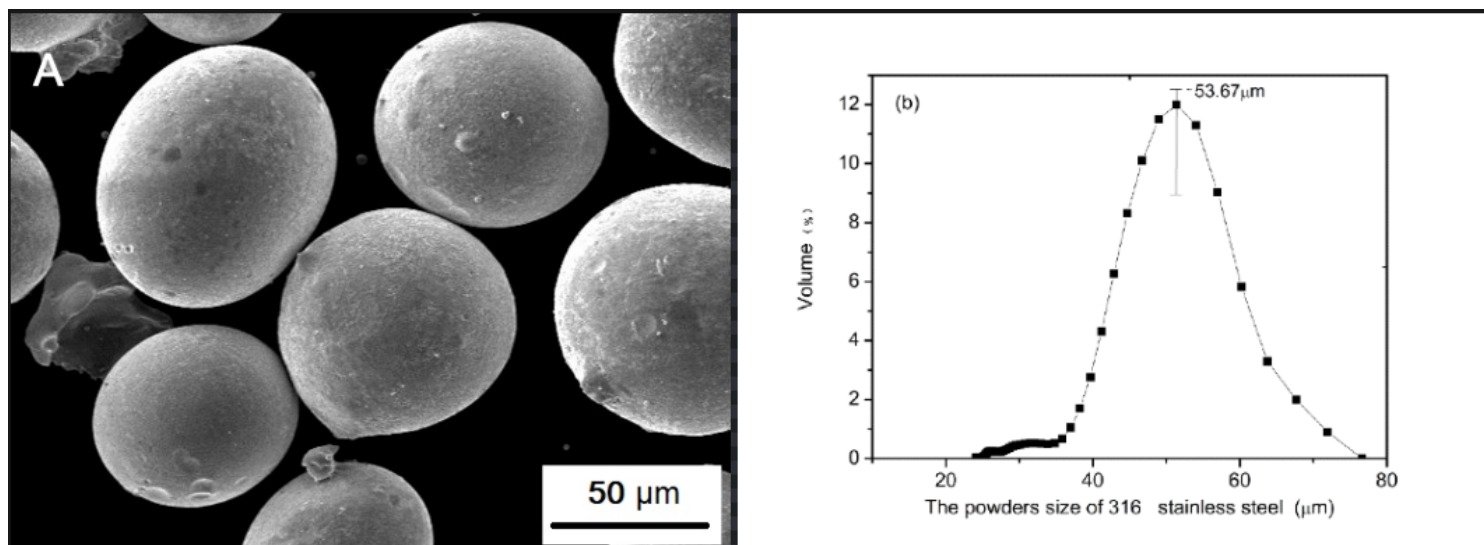


**Figure 1**

Microstructure of the AISI 316 stainless steel powder: (a) SEM image of particles morphology and (b) particle size distribution

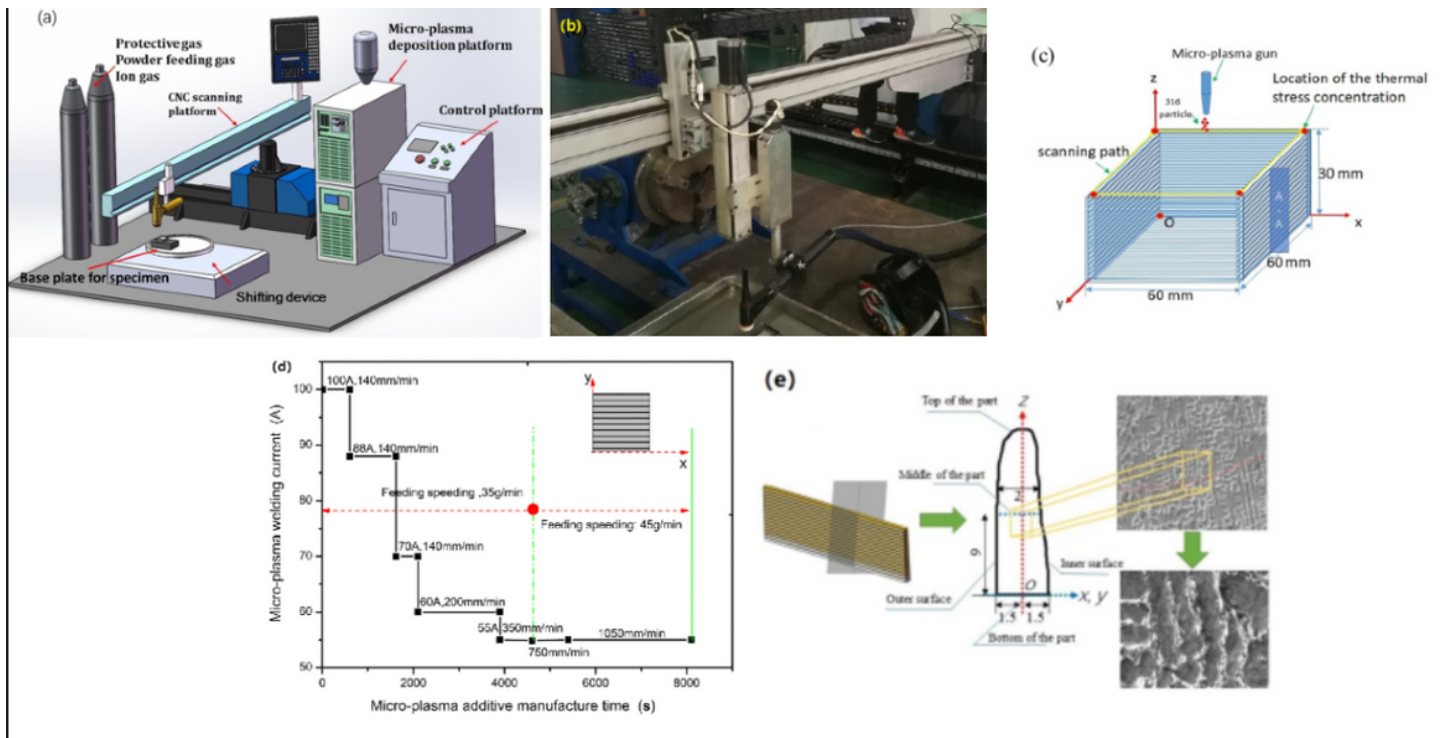


**Figure 2**

(a) Schematic and (b) photograph of the MPAM system; (c) design of the thin-walled AISI 316 stainless steel parts; (d) optimised MPAM process; and (e) 316 stainless steel thin-walled sample taken for microstructural analysis and micro-hardness measurements

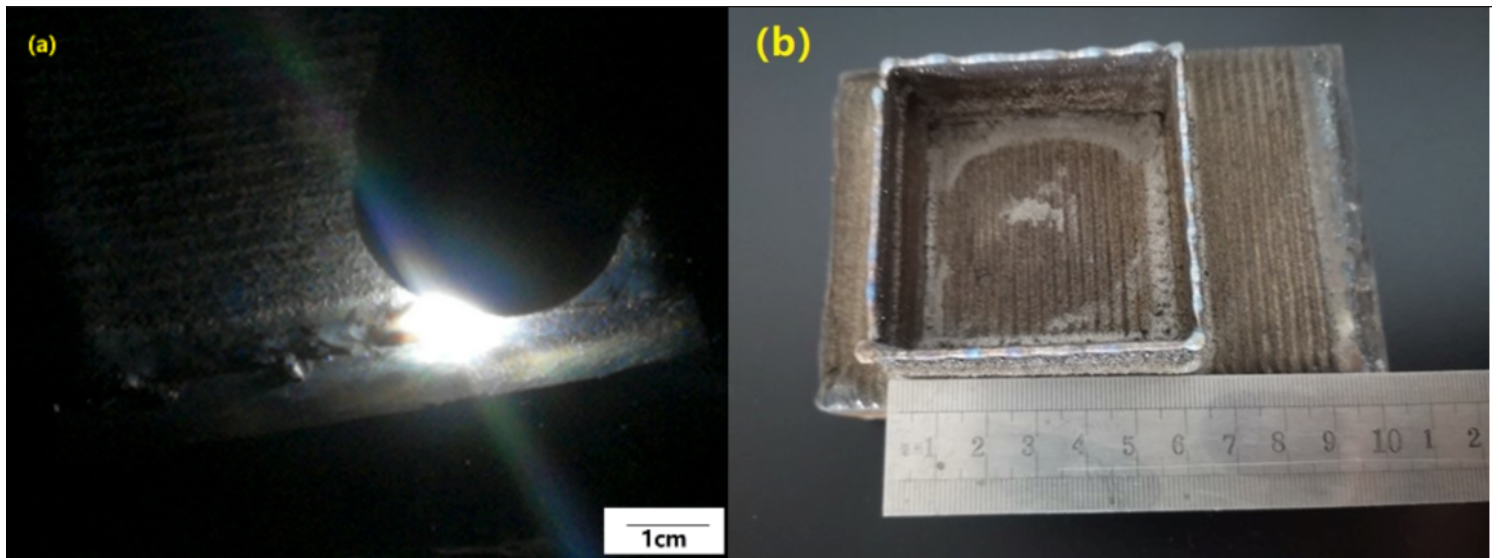


**Figure 3**

Pulsed MPAM process: (a) micro-plasma arc; (b) thin-walled AISI 316 stainless steel made by pulsed MPAM

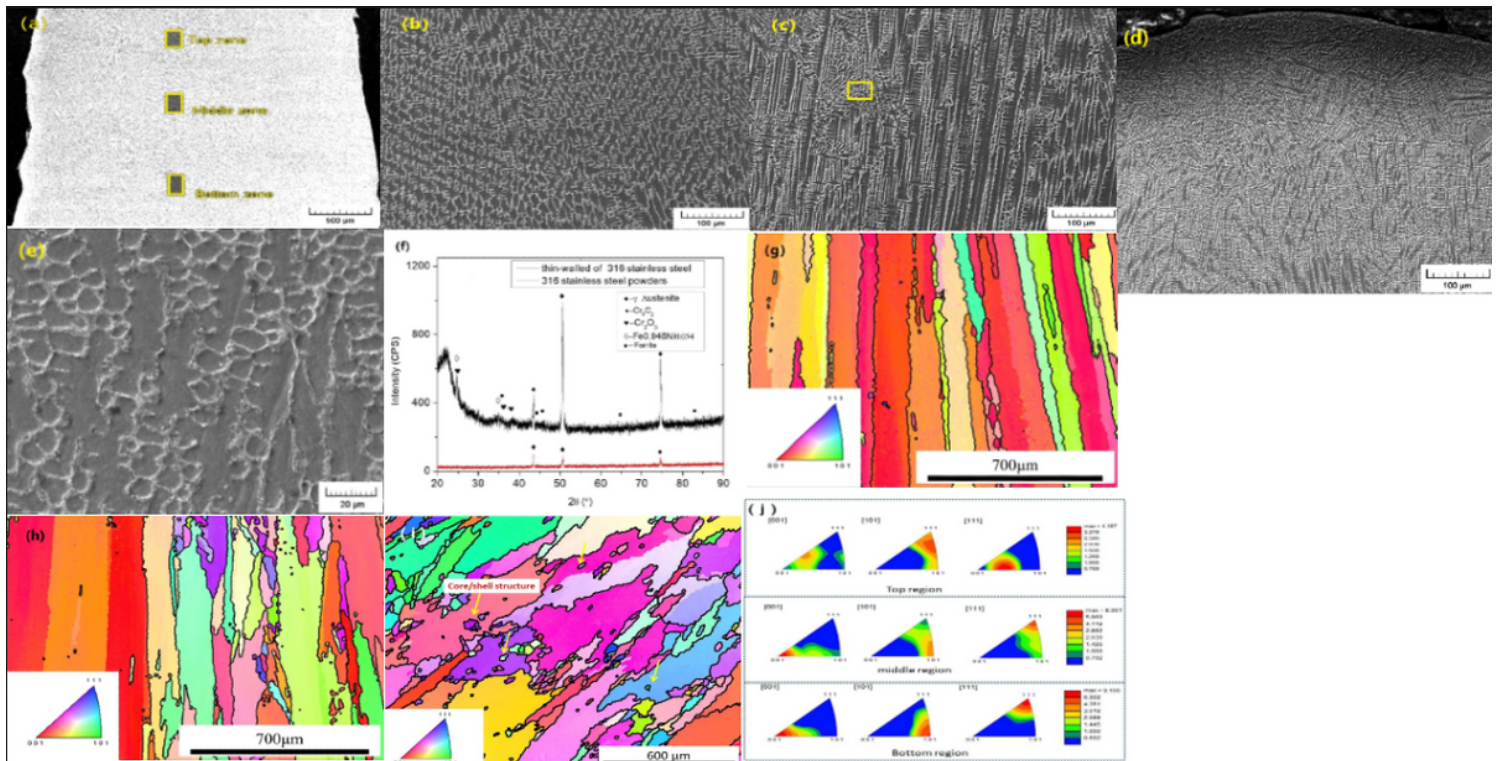


**Figure 4**

microstructure of various positions in the sample of the fabricated parts: (a) low-magnification SE image of the local position, (b) bottom zone of the deposited sample, (c) middle zone of the deposited sample, and (d) top zone of the deposited sample; (e) SEM of the layer zone (in the middle zone, shown in) and (f) XRD pattern of the AISI 316 stainless steel thin-walled parts and powder. (g-i) EBSD of (b, c) and (d), respectively; (j) the inverse pole figures of bottom area and top area, respectively.

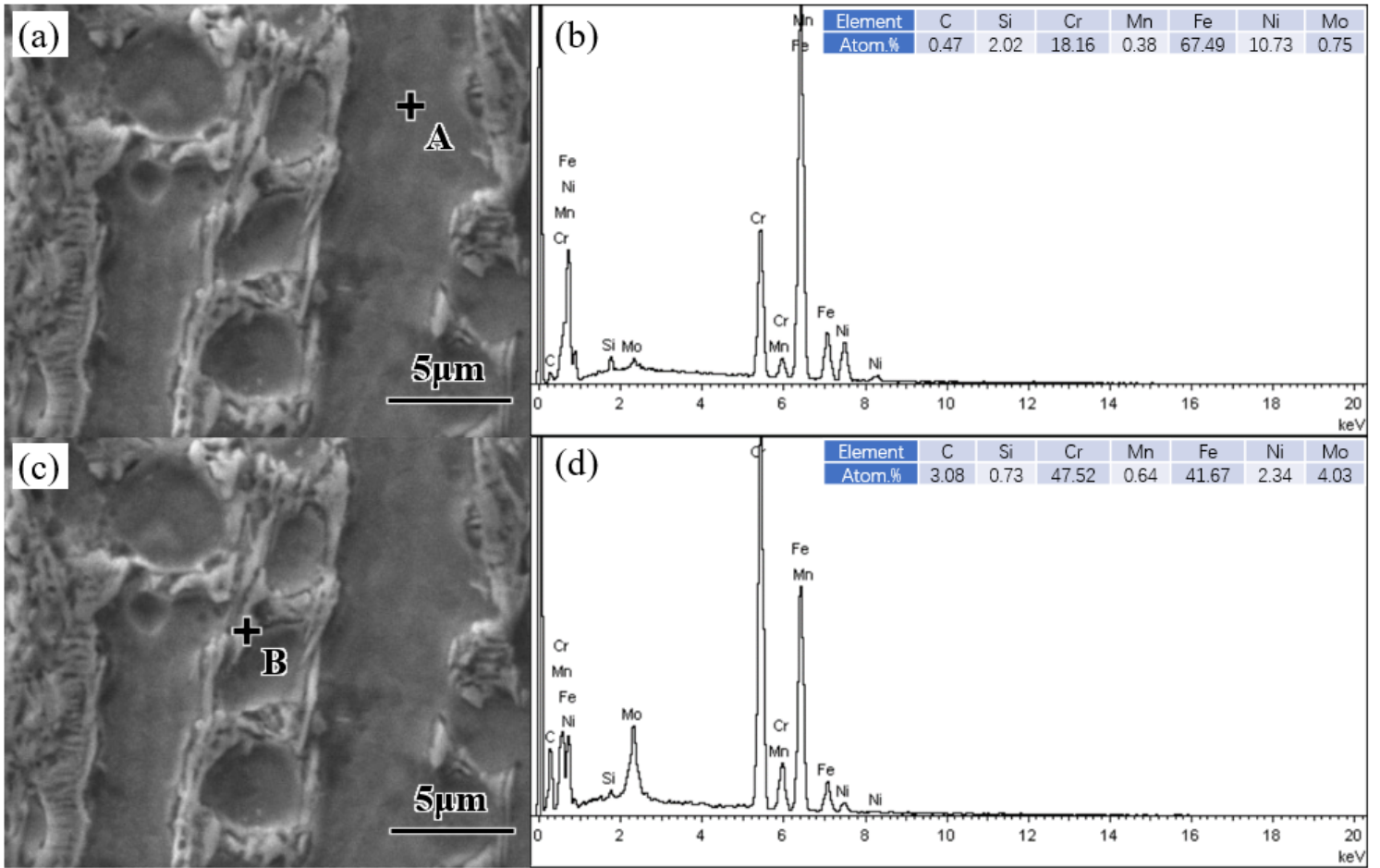


**Figure 5**

(a) SEM image and (b) EDS profile of the dendrite in point A. (c) SEM image and (d) EDS spectrum of the interdendritic region in point B.

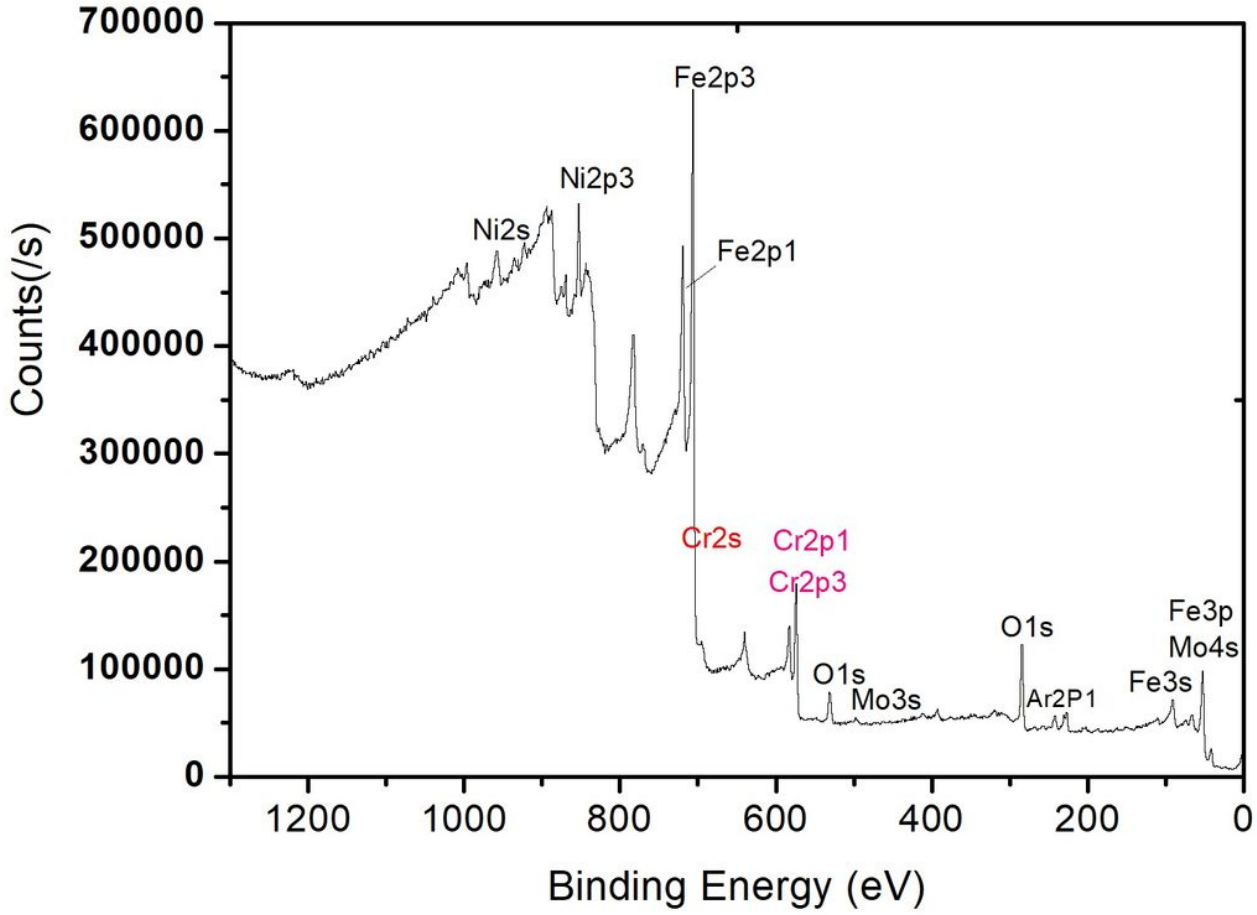
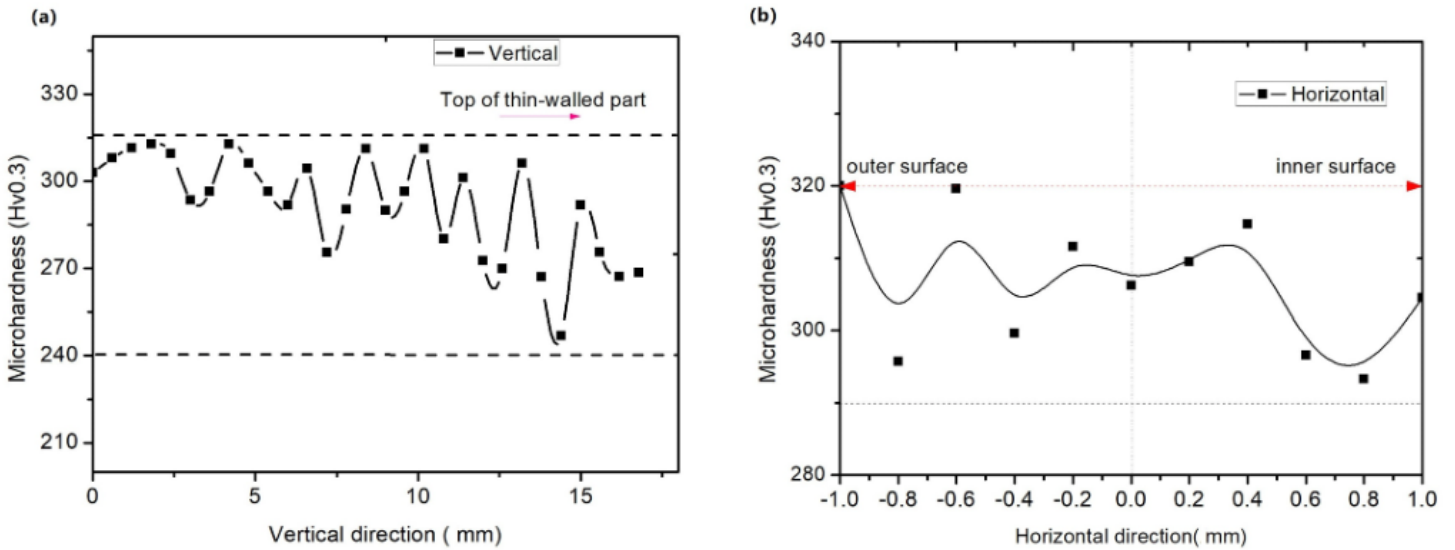


Figure 6

XPS profiles of the surface of the thin-walled AISI 316 stainless steel parts



**Figure 7**

Micro-hardness distribution in the AISI 316 stainless steel parts fabricated by the pulsed MPAM process: hardness distribution in (a) the horizontal direction; (b) the vertical direction

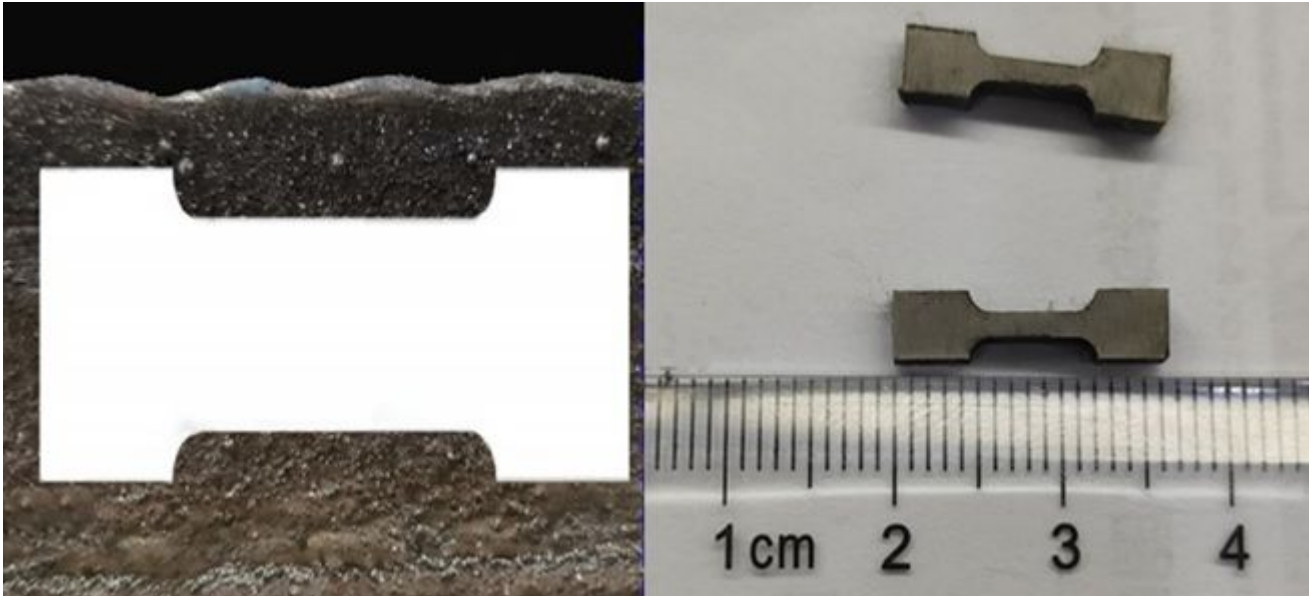


**Figure 8**

Schematic diagram of micro-plasma additive manufacturing parts and sampling and testing dimensions (unit: mm).

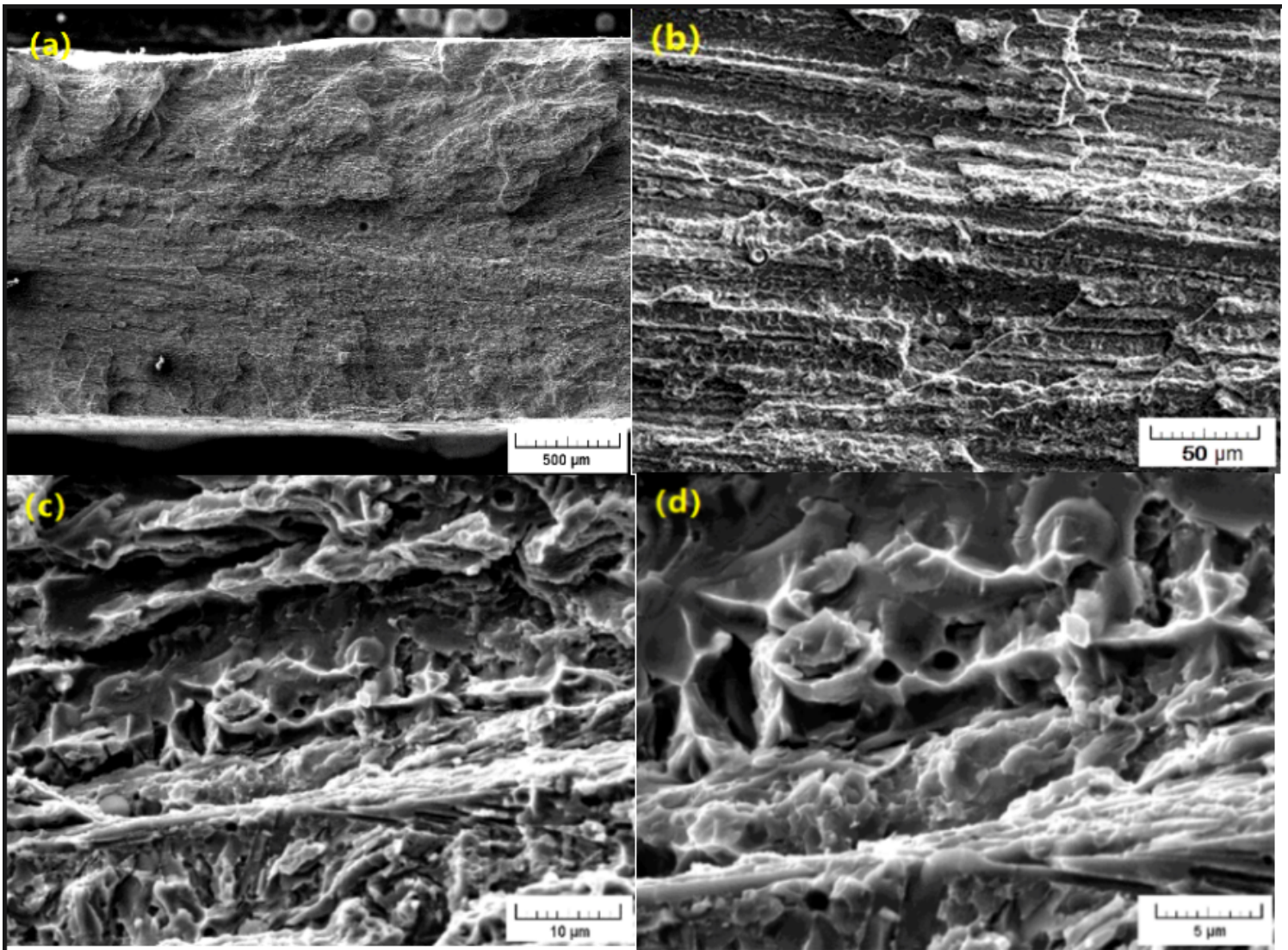


**Figure 9**

Microscopic images revealing the morphology of the fractured sample: (a) fracture surface, (b) dispersed particles in the fracture surface; and (c) and (d) typical dimple-like structure